Anomalous Thermal Transport in Compressed Carbon Phases

Zefang Ye,[*] Janghan Park, Yongjian Zhou, and Raul D. Montano
Walker Department of Mechanical Engineering, The University of Texas at Austin, Austin, Texas 78712, USA

Tribhuwan Pandey[*]
Department of Physics, University of Antwerp, Groenenborgerlaan 171, Antwerp B-2020, Belgium

Yanyao Zhang
Earth and Planetary Sciences, Stanford University, Stanford, California 94305, USA

Jung-Fu Lin[†]
Department of Earth and Planetary Sciences, Jackson School of Geosciences, The University of Texas at Austin, Austin, Texas 78712, USA
and Texas Materials Institute, The University of Texas at Austin, Austin, Texas 78712, USA

Yaguo Wang[‡]
Walker Department of Mechanical Engineering, The University of Texas at Austin, Austin, Texas 78712, USA
and Texas Materials Institute, The University of Texas at Austin, Austin, Texas 78712, USA

(Received 28 February 2024; revised 28 August 2024; accepted 8 October 2024; published 15 November 2024)

Carbon materials display intriguing physical properties, including superconductivity and highly anisotropic thermal conductivity found in graphene. Compressive strain can induce structural and bonding transitions in carbon materials and create new carbon phases, but their interplay with thermal conductivity remains largely unexplored. We investigated the *in situ* high-pressure thermal conductivity of compressed graphitic phases using picosecond transient thermoreflectance and first-principles calculations. Our results show an anomalous thermal conductivity that peaks to 260 W/mK at 15–20 GPa but drops to 3.0 W/mK at ~35 GPa. Together with complimentary *in situ* Raman and x-ray diffraction results, the abnormal thermal conductivity trend of compressed carbon is attributed to phonon-mediated conductivity influenced by interlayer buckling and sp^2 to sp^3 transition and, subsequently, the formation of *M*-carbon nanocrystals and amorphous carbon. Strain-induced structural and bonding variations provide a wide-range manipulation of thermal and mechanical properties in carbon materials.

DOI: 10.1103/PhysRevLett.133.206301

Carbon materials have a diverse range of intriguing physical properties [1,2]. These have inspired a plethora of novel applications, such as combined ultrahardness and toughness for mechanical machining in extreme environments [3,4] and tunable band gap for semiconductors [5,6]. New carbon phases have been discovered over the past decades, such as C60 [7], carbon nanotube [8], and single-layer graphene [9]. These carbon phases, in turn, have been used as the starting materials to enable further discoveries and applications of carbon forms with distinctive properties under extreme environments not accessible at ambient conditions [10–12]. Of particular examples are nanodiamonds with ultrahigh strength exceeding single-crystal diamond [3], Diaphite and Gradia possessing both tetrahedral diamond and layered graphite structures [13,14], and amorphous diamond with unparalleled thermal conductivity compared to other amorphous solids [10,15].

Carbon materials hold a unique position in thermal management because of their wide range of thermal conductivity, from thermal insulation of sensitive devices to rapid cooling of power electronics [1]. The overall thermal conduction of carbon materials can be affected collectively by bond strength, phase, crystallinity, and grain size. Carbon materials can have either or both sp^2 and sp^3 hybridization bonds, which significantly affect the phonon group velocity and hence the thermal conductivity. In crystalline carbon materials, phonons are the primary and highly efficient heat carriers, whereas amorphous materials rely on less efficient vibrational modes like propagons and diffusons [16]. The presence of grain boundaries in polycrystalline materials introduces additional phonon scattering channels, resulting in a strong dependence of thermal conductivity on grain size [17].

[*]These authors contributed equally to this work.
[†]Contact author: afu@jsg.utexas.edu
[‡]Contact author: yaguo.wang@austin.utexas.edu

Diamond has the highest thermal conductivity of 2450 W/mK [18], from the strong sp^3 hybridization, highly symmetric cubic structure, and minimal effects by grain boundaries and defects. Nanocrystal diamond, on the other hand, has a wide thermal conductivity range, from 278 to less than 1 W/mK, due to the grain boundary scattering [17]. Amorphous carbon can have a thermal conductivity as low as less than 1 W/mK, with mixed sp^2/sp^3 hybridization and disordered atomic arrangement that disrupt phonon propagation for heat transport [19]. As a special case, graphite has highly anisotropic thermal conductivity: about 2130 W/mK along the in-plane direction with sp^2 hybridization and 6.36 W/mK along the cross-plane direction with weak van der Waals force [18], highlighting the influence of bond strength on conductivity. Previous studies have shown that carbon materials under extreme pressure can undergo structural phase transitions, sp^2 to sp^3 bond conversion, and/or grain size reduction [20]. That means compressive strain can be used to effectively manipulate the thermal conductivity of carbon materials. Even though the relations between thermal conductivity and structural factors (e.g., phases, bonds, crystallinity, and grain sizes) in carbon materials have been studied at ambient conditions, the magnitudes of their interplays in highly compressed carbon phases are largely unexplored. It is thus crucial to investigate and interpret the thermal conductivity with complimentary structural results to establish a coherent understanding of carbon materials at extremes.

In this study, our objective is to measure and predict the thermal conductivity in high-pressure carbon phases and understand how the structural changes would qualitatively influence the thermal transport behavior. This is achieved by monitoring changes in both thermal conductivity and structural characteristics in highly oriented pyrolytic graphite (HOPG) compressed in a diamond anvil cell (DAC) at room temperature. *In situ* thermal conductivity measurements in a DAC, employing picosecond transient thermoreflectance spectroscopy (ps-TTR) [21], reveal a complex trend with rapid increase and sudden drop in high-pressure carbon phases, along with structural transition from graphite, to a mixed phase of *M*-carbon nanocrystals surrounded by amorphous carbon, as revealed with *in situ* x-ray diffraction (XRD) and Raman spectroscopy. First-principles density functional theory (DFT) calculations dissect the aforementioned factors from structure changes and establish a connection to the observed thermal conductivity variation.

HOPG is chosen as the starting material due to its high-quality crystallinity and confirmed structural transitions under compression [22]. A schematic picture of the thermal conductivity measurement within the DAC is shown in Fig. 1(a), the same setup has been applied to study the pressure-dependent thermal transport of MoS_2 [23]. Plotted in Fig. 1(b) are the normalized time-dependent reflectance

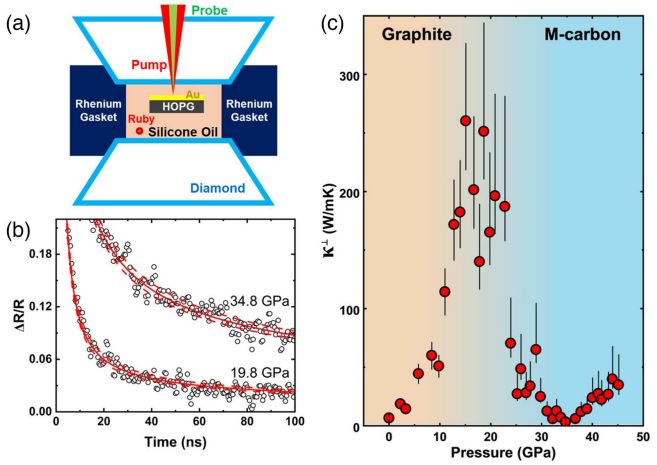

FIG. 1. Cross-plane thermal conductivity experiments in compressed HOPG using ps-TTR coupled with a DAC. (a) Schematic of the experimental geometry with a DAC integrated into a ps-TTR system. (b) Normalized experimental data and their best-fitted curves (solid red lines) with a ±20% confidence interval (dashed red lines) at two selected pressures. (c) Extracted pressure-dependent thermal conductivity. Two shaded areas mark the two possible phases as suggested in the literature [22].

changes at two selected pressures. To extract thermal conductivity, a 1D heat conduction model is used to fit the experimental data, represented by the red solid lines, along with a ±20% confidence interval. The extracted pressure-dependent cross-plane thermal conductivities ($\kappa^{\perp}$) with uncertainties are plotted in Fig. 1(c). At ambient pressure, the $\kappa^{\perp}$ value is about 6.4 W/mK. Under compression, the pressure-dependent trend of $\kappa^{\perp}$ displays a complex feature. Initially at pressures below 11 GPa, $\kappa^{\perp}$ steadily increases with pressure. Above 11 GPa, a sudden and rapid increase is observed, and the peak value of $\kappa^{\perp}$ is at approximately 260 W/mK at the pressure range of 15–20 GPa. This is about 40 times higher than the $\kappa^{\perp}$ value at ambient pressure. Above 20 GPa, $\kappa^{\perp}$ shows a quick drop to values even lower than at ambient, with a dip appearing around 35 GPa (~3.0 W/mK). Above 36 GPa, $\kappa^{\perp}$ starts to increase again and tends to saturate around 45 GPa. Previous works on the structure changes in compressed HOPG suggested that about half of the π bonds transitioned to σ-bonds at around 17 GPa [24] and the possible formation of the *M*-carbon phase at around 19.2 GPa [22], which are indicated by shaded areas in Fig. 1(c). The complex features of $\kappa^{\perp}$ suggests that several competing factors at play under pressure, rather than a straight transition from graphite to *M*-carbon.

To gain more insights into the thermal transport evolution, we conducted *in situ* XRD and Raman spectroscopy on the compressed HOPG (Fig. 2). The inset of Fig. 2(a) displays two representative XRD patterns of the sample along with the d-spacing evolution of the (002) cross-plane orientation. At 1.7 GPa, the XRD spectrum is typical for the

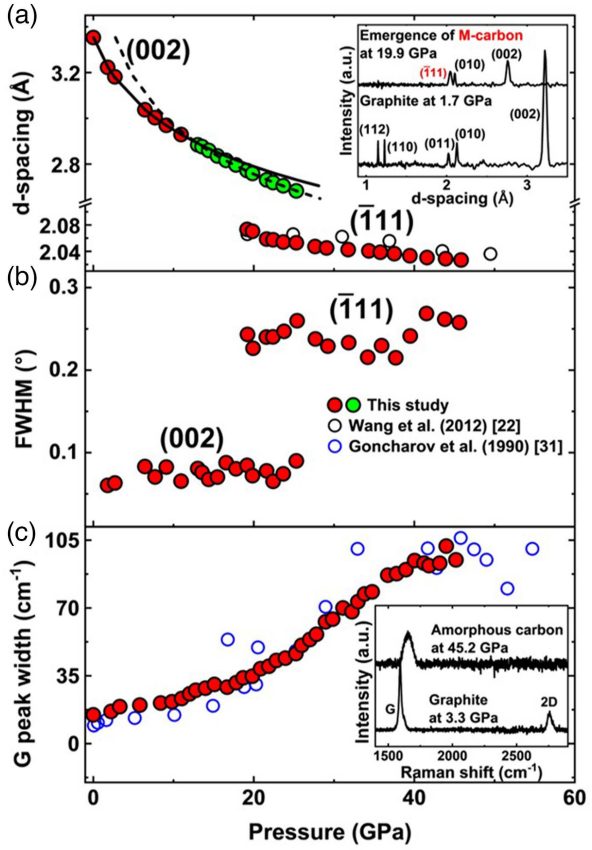

FIG. 2. *In situ* structural characterization of pressed HOPG. (a) Pressure-dependent d spacings of graphite HOPG and M-carbon $(1\bar{1}1)$ plane. The solid line represents fitting with the third-order finite-strain equation of state, and the dashed line is for eye guidance of deviation from the fitting above 11 GPa. (Inset) Processed XRD spectra at various pressures. (b) Pressure-dependent FWHM of M-carbon $(1\bar{1}1)$ and graphite (002) peaks. (c) Raman G peak FWHM evolution under pressure. (Inset) Raman spectra at 3.3 and 45.2 GPa.

graphite phase, where the (002) peak is related to the graphite interlayer distance. Above 19 GPa, a new peak emerges between peaks (011) and (010), and this peak's position is consistent with the occurrence of M-carbon [marked as $(1\bar{1}1)$] [22]. This becomes the sole peak above 25 GPa, indicating the complete disappearance of the original graphite phase [Figs. S6(e)–S6(f) [25]]. Figure 2(a) plots the interlayer d spacing extracted from the graphite peak (002), which is fitted using the third-order finite-strain equation of state (EOS) [51]. The axial incompressibility of cross-plane graphite extracted from the linear EOS fit is approximately 35.4 GPa, with an interlayer spacing of 3.36 Å, consistent with the literature [22,52]. Beyond 11 GPa, experimental results deviate from the linear EOS extended to higher pressure, indicating higher compressibility, which can be explained by the strengthening of the interlayer bonding drawing the layers closer. As shown in Figs. 2(b) and S6(h) [25], the FWHM of the M-carbon $(1\bar{1}1)$ peak is much greater than that of HOPG and remains unchanged with pressure. Using the Scherrer equation [53], we estimate the average grain size of M-carbon to be roughly about 10 nm. This value may have a large uncertainty because only one single XRD peak was used for the estimation. However, it qualitatively reveals the nanocrystalline nature and significant grain size reduction associated with the formation of M-carbon phase [Fig. 2(b)].

The G peak, which corresponds to the in-plane E_{2g} mode at the Γ point, in *in situ* Raman spectra provides additional insights into structure change, which corresponds to the in-plane E_{2g} modes at the Γ point. As expected from the bond strengthening under compression, the G peak position displays the blue shift with pressure [inset of Fig. 2(c), Fig. S8(b) [25]]. The FWHM of the G peak is reported to be proportional to the bond-angle disorder at sp^2 sites [54]. Below 11 GPa, the FWHM width only shows a slight increase, suggesting that compression at this pressure range only causes slight distortion between layers, e.g., interlayer sliding and/or lattice rotation. Above 11 GPa, FWHM increases linearly until 25 GPa and then continues with an even higher rate until 36 GPa and then saturates. The rapid increase above 11 GPa is strong evidence of an in-plane disordering process that persists until 36 GPa. Based on previous studies [22,55,56], this disorder could be caused by interlayer buckling, the formation of M-carbon nanocrystals, as well as amorphization. We note that amorphization has been observed in several studies of compressed graphite [55,56]. Combining the results of XRD and Raman, we propose that the final high-pressure structure of compressed HOPG includes M-carbon nanocrystals embedded in amorphous carbon, both of which can have significant impacts on thermal conductivity.

Analyses of XRD and Raman results and previous studies [22,24,55,56] reveal a number of structure changes in compressed graphite: bond shortening before 11 GPa, the formation of interlayer σ bonds at 11–20 GPa, and the emergence of M-carbon nanocrystals along with amorphous carbon after 19 GPa. To understand how those structure changes affect the phonon properties and the overall thermal conductivity, we performed the first-principles calculations along with phonon Boltzmann transport equations (PBTE). With PBTE, the lattice thermal conductivity (κ) is given by $\kappa = (1/NV)\sum_\lambda C_\lambda v_\lambda^\alpha v_\lambda^\alpha \tau_\lambda^\alpha$, where λ denotes a phonon mode in branch p with wave vector $\mathbf{q}$, C_λ is the volumetric specific heat, v_λ^α is the phonon group velocity, and τ_λ^α is the phonon lifetime in the α^{th} direction. N is the number of $\mathbf{q}$ points uniformly sampled in the Brillouin zone, and V is the volume of the unit cell. Figures 3(a) and 3(b) display the phonon dispersion of graphite and M-carbon. In contrast to the interlayer vdW force in graphite, sp^3 hybridization in M-carbon shifts the phonon dispersion towards a more 3D-like form, resulting in a larger phonon density of states (DOS)

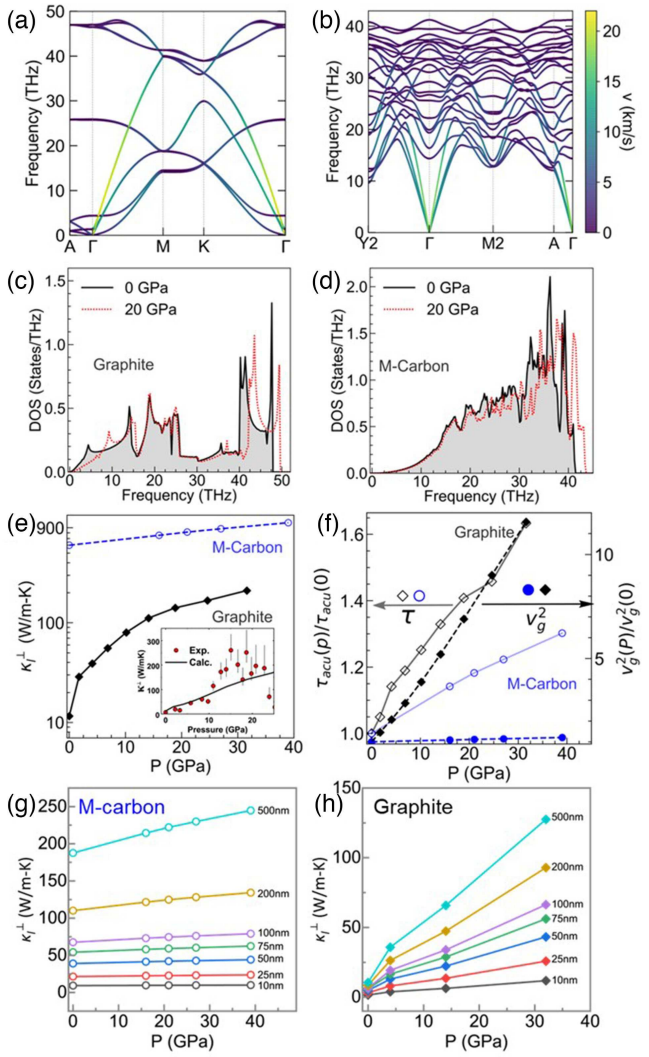

FIG. 3. First-principles calculations of phonon and thermal behaviors in graphite and *M*-carbon. Phonon dispersion and phonon group velocities in (a) graphite and (b) *M*-carbon. Phonon density of state at 0 and 20 GPa for (c) graphite and (d) *M*-carbon. (e) Pressure-dependent thermal conductivity of graphite and *M*-carbon. Inset: comparison of graphite thermal conductivity between the calculations and experiments. (f) Pressure-dependent relative change in the square of group velocity (right *Y* axis) and phonon lifetime (left *Y* axis) for graphite and *M*-carbon with respect to 0 GPa values. (g) Pressure-dependent thermal conductivity of *M*-carbon nanocrystals with varying crystal size. (h) Pressure-dependent thermal conductivity of graphite nanocrystals with varying crystal size.

[see Figs. 3(c) and 3(d)] and higher phonon group velocity. This enhances $\kappa^{\perp}$ in *M*-carbon by several orders of magnitude higher than that of graphite. As evident from Figs. 3(c) and 3(d), the phonon DOS of graphite is suppressed in the 0–8 THz range under the application of pressure. However, the phonon DOS of *M*-carbon remains largely unaffected in the low-frequency region. This behavior can be attributed to the relatively weaker interlayer bonding in graphite compared to *M*-carbon, which makes it more susceptible to compression.

Figure 3(e) compares the pressure-dependent $\kappa^{\perp}$ of graphite and *M*-carbon, where graphite shows 20 times increase from 10 to about 200 W/mK at 30 GPa, with the increasing trend saturating at high pressure. For *M*-carbon, an almost linear trend is observed with 50% increase of $\kappa^{\perp}$ from 600 to 900 W/mK at 30 GPa. The difference in pressure-dependent $\kappa^{\perp}$ in graphite and *M*-carbon can be attributed to the greater tunability in graphite due to its weak interlayer vdW bonding. As depicted in Fig. 3(f), the pressure-dependent relative changes in phonon lifetime and group velocity square are more significant in graphite. The inset of Fig. 3(e) presents a comparison between the simulated thermal conductivity trends of the H-graphite phase and experimental data. The simulations align closely with experimental results below 11 GPa, prior to the onset of interlayer buckling. However, once the interlayer bonding begins, the experimental thermal conductivity significantly surpasses the simulated values. Figures 3(g) and 3(h) illustrate the size effect on the pressure-dependent thermal conductivity for both *M*-carbon and graphite. It is evident that the thermal conductivity of *M*-carbon shows no significant dependence on pressure when the crystal size is below 25 nm. In contrast, for graphite, a pronounced pressure dependence is observed even when the crystal size is as small as 10 nm.

Figure 4(a) summarizes the thermal conductivity values of some representative carbon materials reported in literature and compares them with our results. Previous studies use either phase synthesis [e.g., diamond, graphite, amorphous diamond (AD)] [1] or grain size [nanopolycrystalline diamond (NPD)] [17] to manipulate thermal conductivity of carbon materials. Pressure can tune multiple competing factors (bond strength, phase, crystallinity, and grain size) simultaneously with great flexibility. Figure 4(b) illustrates how these factors affect the phonon properties. At the low pressure regime (blue region marked with HOPG), $\kappa^{\perp}$ monotonically increases with pressure, similar to the trend predicted with PBTE [Fig. 3(e)]. *In situ* XRD suggests that the graphite phase is preserved during this pressure range, with the interlayer distance shrinking continuously. First-principles calculations [Fig. 3(f)] reveal that the main reason for the increase in thermal conductivity is the higher phonon group velocity resulting from enhanced interlayer interactions, as depicted in Fig. 4(b) for pressure less than 11 GPa. When pressure increases, a sudden rapid increase of $\kappa^{\perp}$ is observed, and a peak appears in the pressure range of 15–20 GPa. Analysis of XRD data [Fig. 2(a)] shows that at around 11 GPa, the *d* spacing corresponding to the interlayer distance starts to deviate from the EOS fitting. The FWHM of the Raman *G* peak increases rapidly in this pressure regime, indicating distortion along the in-plane direction. Both findings suggest that interlayer buckling with the transition from sp^2 to sp^3 (from the formation of

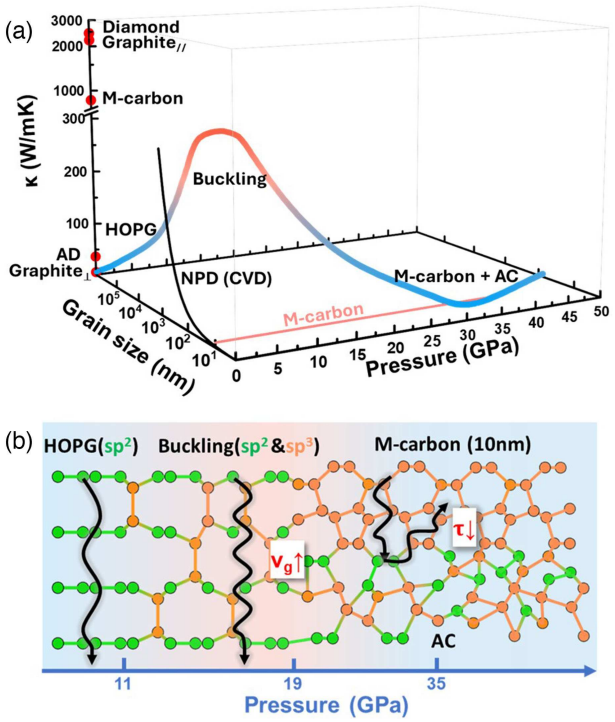

FIG. 4. The schematic diagrams of thermal conductivity and structure change of HOPG under pressure. (a) Schematic picture illustrating the tunability of HOPG thermal conductivity under pressure. For comparison, literature values of diamond, in-plane graphite, cross-plane graphite [18], amorphous diamond [15], and M-carbon (PBTE calculation) are plotted as red dots. Grain-size dependent κ of nanopolycrystalline diamond is shown as the black curve [17]. (b) The illustrations of the underlying mechanism, during the early stages of the phase transition, enhanced thermal conductivity is driven by increased phonon group velocity, a consequence of interlayer bonding. Subsequently, the formation of the post-transition phase involving the 10 nm M-carbon and amorphous carbon reduces phonon lifetime, ultimately leading to thermal conductivity suppression.

interlayer σ bonds) occurs. The measured $\kappa^{\perp}$ values increase much faster than those predicted by first-principles calculations [inset of Fig. 3(e)], the latter of which does not consider any interlayer buckling effect. Interlayer buckling induces covalent bonds in atoms across layers, significantly stronger than vdW bonding, which greatly enhances the phonon group velocity along the cross-plane direction and results in the rapid increase of $\kappa^{\perp}$. The pressure region corresponding to the peak $\kappa^{\perp}$ value, 15–20 GPa, with values of more than 260 W/mK, about 40 times the $\kappa^{\perp}$ value at ambient pressure. This pressure range is close to the range where approximately half of sp^2 bond transits to sp^3 bond [24]. At intermediate pressure (> 20 GPa), $\kappa^{\perp}$ shows a quick decrease to ~3.0 W/mK, even lower than that of ambient pressure. Analysis of XRD data further suggests the formation of M-carbon nanocrystals above 19 GPa. The appearance of the M-carbon phase has the potential to continuously increase thermal conductivity [bulk $\kappa^{\perp} > 600$ W/mK, Fig. 3(e)]. However, the nanocrystalline structure of M-carbon demonstrates significant phonon-grain boundary scattering, leading to a markedly lower thermal conductivity [Fig. 3(g)]. The pink line in Fig. 4(a) represents the calculated of 10 nm M-carbon nanocrystal, with an almost constant value of 9.3 W/mK for all pressure. This pressure-independent behavior is observed across all M-carbon nanocrystals with sizes below 25 nm [Fig. 3(g)]. Therefore, attributing the dip and subsequent increase solely to the formation of M-carbon nanocrystals is insufficient for a complete explanation. The observed low thermal conductivity value around the dip can be attributed to the presence of amorphous carbon, which typically exhibits a thermal conductivity of less than 3.5 W/mK. As illustrated in Fig. 4(b), the existence of amorphous carbon can disrupt and even eliminate phonon propagation, and phonons in M-carbon nanocrystals can be strongly scattered at the interface between M-carbon and amorphous carbon. In the high-pressure regime (> 35 GPa), the phase transition is complete, $\kappa^{\perp}$ starts to increase again and tends to saturate around 45 GPa. Since 10 nm M-carbon nanocrystal is insensitive to pressure, this increase mainly comes from the transition from sp^2 to sp^3 bonding in amorphous carbon (Sec. V in Supplemental Material [25]).

In summary, we have investigated the *in situ* $\kappa^{\perp}$ of compressed HOPG with ps-TTR. Unlike the previous work about MoS_2, where thermal conductivity only shows a monotonic increase due to the strengthened interlayer force under pressure, here we observed a complex trend of thermal conductivity changes from 6.4 W/mK at ambient pressure to a peak value of 260 W/mK at 15–20 GPa, and then drops to 3.0 W/mK at around 35 GPa. Raman and x-ray diffraction scattering results reveal pressure-induced structure transitions, formation of sp^3 bonds and grain-size reduction, all of which can drastically affect thermal conductivity of compressed carbon phases. First-principles calculations suggest that thermal conductivity of the high-pressure phases is highly tunable due to pressure-induced changes in phonon group velocity and lifetime and suggest that the rapid increase at low to intermediate pressure regime is attributed to interlayer buckling and sp^2 to sp^3 hybridization transition, and the sudden drop at high pressure comes from formation of M-carbon nanocrystals and amorphization. Of particular interest is the observation of the peaked thermal conductivity of ~260 W/mK with mixed phases of interlayer-buckled graphite and nanocrystal M-carbon at 15–20 GPa [Fig. 4(b)]. These mixed phases are also expected to exhibit ultrahigh hardness [24], along with wide electronic band gap and high thermal conductivity. Compared with traditional approaches to manipulate thermal conductivity under ambient conditions, applying pressure allows a wide-range manipulation of multiple parameters simultaneously that make it possible to realize desirable thermal conductivity along with other

novel properties. This study represents the first *in situ* examination of co-evolution of thermal transport and structural factors (phases, bonds, crystallinity, and grain size) in graphitic materials under high pressure. It is conceivable that one can search for a wide range of thermal transport properties in various structural arrangements by using different starting carbon materials (e.g. multilayer graphene, CNT, C60) for high-pressure experiments. This in turn opens vast opportunities to tailor design carbon phases with desirable thermal, electronic, mechanical, and optical properties for thermal management, semiconductor, and mechanical machining applications.

Acknowledgments—Sincere appreciation to Dr. Stella Chariton and Dr. Vitali B. Prakapenka at Argonne National Lab for assisting the high-pressure x-ray diffraction experiments. This work was supported by the National Science Foundation (CBET- 2211660 and DMR-2132574).

[1] A. A. Balandin, Thermal properties of graphene and nanostructured carbon materials, Nat. Mater. **10**, 569 (2011).
[2] A. Hirsch, The era of carbon allotropes, Nat. Mater. **9**, 868 (2010).
[3] T. Irifune, A. Kurio, S. Sakamoto, T. Inoue, and H. Sumiya, Ultrahard polycrystalline diamond from graphite, Nature (London) **421**, 599 (2003).
[4] Q. Huang, D. Yu, B. Xu, W. Hu, Y. Ma, Y. Wang, Z. Zhao, B. Wen, J. He, Z. Liu *et al.*, Nanotwinned diamond with unprecedented hardness and stability, Nature (London) **510**, 250 (2014).
[5] Y. Zhang, T.-T. Tang, C. Girit, Z. Hao, M. C. Martin, A. Zettl, M. F. Crommie, Y. R. Shen, and F. Wang, Direct observation of a widely tunable bandgap in bilayer graphene, Nature (London) **459**, 820 (2009).
[6] C. H. Lui, Z. Li, K. F. Mak, E. Cappelluti, and T. F. Heinz, Observation of an electrically tunable band gap in trilayer graphene, Nat. Phys. **7**, 944 (2011).
[7] H. W. Kroto, J. R. Heath, S. C. O'Brien, R. F. Curl, and R. E. Smalley, C60: Buckminsterfullerene, Nature (London) **318**, 162 (1985).
[8] S. Iijima, Helical microtubules of graphitic carbon, Nature (London) **354**, 56 (1991).
[9] K. S. Novoselov, A. K. Geim, S. V. Morozov, D.-e. Jiang, Y. Zhang, S. V. Dubonos, I. V. Grigorieva, and A. A. Firsov, Electric field effect in atomically thin carbon films, Science **306**, 666 (2004).
[10] Y. Shang, Z. Liu, J. Dong, M. Yao, Z. Yang, Q. Li, C. Zhai, F. Shen, X. Hou, L. Wang *et al.*, Ultrahard bulk amorphous carbon from collapsed fullerene, Nature (London) **599**, 599 (2021).
[11] Z. Wang, Y. Zhao, K. Tait, X. Liao, D. Schiferl, C. Zha, R. T. Downs, J. Qian, Y. Zhu, and T. Shen, A quenchable superhard carbon phase synthesized by cold compression of carbon nanotubes, Proc. Natl. Acad. Sci. U.S.A. **101**, 13699 (2004).
[12] L. G. P. Martins, M. J. Matos, A. R. Paschoal, P. T. Freire, N. F. Andrade, A. L. Aguiar, J. Kong, B. R. Neves, A. B. de Oliveira, M. S. Mazzoni *et al.*, Raman evidence for pressure-induced formation of diamondene, Nat. Commun. **8**, 96 (2017).
[13] P. Németh, H. J. Lancaster, C. G. Salzmann, K. McColl, Z. Fogarassy, L. A. Garvie, L. Illés, B. Pécz, M. Murri, F. Corà *et al.*, Shock-formed carbon materials with intergrown sp3-and sp2-bonded nanostructured units, Proc. Natl. Acad. Sci. U.S.A. **119**, e2203672119 (2022).
[14] K. Luo, B. Liu, W. Hu, X. Dong, Y. Wang, Q. Huang, Y. Gao, L. Sun, Z. Zhao, Y. Wu *et al.*, Coherent interfaces govern direct transformation from graphite to diamond, Nature (London) **607**, 486 (2022).
[15] Y. Shang, M. Yao, Z. Liu, R. Fu, L. Yan, L. Yang, Z. Zhang, J. Dong, C. Zhai, X. Hou *et al.*, Enhancement of short/medium-range order and thermal conductivity in ultrahard sp3 amorphous carbon by C70 precursor, Nat. Commun. **14**, 7860 (2023).
[16] P. B. Allen, J. L. Feldman, J. Fabian, and F. Wooten, Diffusons, locons and propagons: Character of atomie yibrations in amorphous Si, Philos. Mag. B **79**, 1715 (1999).
[17] M. A. Angadi, T. Watanabe, A. Bodapati, X. Xiao, O. Auciello, J. A. Carlisle, J. A. Eastman, P. Keblinski, P. K. Schelling, and S. R. Phillpot, Thermal transport and grain boundary conductance in ultrananocrystalline diamond thin films, J. Appl. Phys. **99**, 114301 (2006).
[18] C. Ho, R. Powell, and P. Liley, Thermal conductivity of the elements: A comprehensive review, J. Phys. Chem. Ref. Data **3**, 11974 (1974).
[19] A. J. Bullen, K. E. O'Hara, D. G. Cahill, O. Monteiro, and A. Von Keudell, Thermal conductivity of amorphous carbon thin films, J. Appl. Phys. **88**, 6317 (2000).
[20] B. Sundqvist, Carbon under pressure, Phys. Rep. **909**, 1 (2021).
[21] J. Jeong, X. Meng, A. K. Rockwell, S. R. Bank, W.-P. Hsieh, J.-F. Lin, and Y. Wang, Picosecond transient thermoreflectance for thermal conductivity characterization, nanoscale microscale, Thermophys. Eng. **23**, 211 (2019).
[22] Y. Wang, J. E. Panzik, B. Kiefer, and K. K. Lee, Crystal structure of graphite under room-temperature compression and decompression, Sci. Rep. **2**, 520 (2012).
[23] X. Meng, T. Pandey, J. Jeong, S. Fu, J. Yang, K. Chen, A. Singh, F. He, X. Xu, J. Zhou *et al.*, Thermal conductivity enhancement in MoS_2 under extreme strain, Phys. Rev. Lett. **122**, 155901 (2019).
[24] W. L. Mao, H.-k. Mao, P. J. Eng, T. P. Trainor, M. Newville, C.-c. Kao, D. L. Heinz, J. Shu, Y. Meng, and R. J. Hemley, Bonding changes in compressed superhard graphite, Science **302**, 425 (2003).
[25] See Supplemental Material at http://link.aps.org/supplemental/10.1103/PhysRevLett.133.206301 for the experiment and calculation details, which includes Refs. [26–50].
[26] A. Dewaele, M. Torrent, P. Loubeyre, and M. Mezouar, Compression curves of transition metals in the Mbar range: Experiments and projector augmented-wave calculations, Phys. Rev. B **78**, 104102 (2008).
[27] W.-P. Hsieh, Thermal conductivity of methanol-ethanol mixture and silicone oil at high pressures, J. Appl. Phys. **117**, 235901 (2015).
[28] S.-H. Shim, T. S. Duffy, and K. Takemura, Equation of state of gold and its application to the phase boundaries near

660 km depth in Earth's mantle, Earth Planet. Sci. Lett. **203**, 729 (2002).
[29] G. T. Hohensee, M. R. Fellinger, D. R. Trinkle, and D. G. Cahill, Thermal transport across high-pressure semiconductor-metal transition in Si and Si 0.991 Ge 0.009, Phys. Rev. B **91**, 205104 (2015).
[30] Y. Touloukian and E. Buyco, Thermophysical properties of matter-the TPRC data series. volume 4. specific heat-metallic elements and alloys (1971), https://www.osti.gov/biblio/5439707.
[31] Y. Touloukian, R. Powell, C. Ho, and P. Klemens, Thermophysical properties of matter-the TPRC data series. Volume 1. Thermal conductivity-metallic elements and alloys (1970), https://www.osti.gov/biblio/5447756.
[32] X. Wang, Z. Bao, Y. Zhang, F. Li, R. Yu, and C. Jin, High pressure effect on structural and electrical properties of glassy carbon, J. Appl. Phys. **93**, 1991 (2003).
[33] Q. Li, Y. Ma, A. R. Oganov, H. Wang, H. Wang, Y. Xu, T. Cui, H.-K. Mao, and G. Zou, Superhard monoclinic polymorph of carbon, Phys. Rev. Lett. **102**, 175506 (2009).
[34] Y. X. Zhao and I. L. Spain, X-ray diffraction data for graphite to 20 GPa, Phys. Rev. B **40**, 993 (1989).
[35] G. Kresse and J. Furthmüller, Efficiency of *ab initio* total energy calculations for metals and semiconductors using a plane-wave basis set, Comput. Mater. Sci. **6**, 15 (1996).
[36] G. Kresse and D. Joubert, From ultrasoft pseudopotentials to the projector augmented-wave method, Phys. Rev. B **59**, 1758 (1999).
[37] P. E. Blöchl, Projector augmented-wave method, Phys. Rev. B **50**, 17953 (1994).
[38] J. P. Perdew, K. Burke, and M. Ernzerhof, Generalized gradient approximation made simple, Phys. Rev. Lett. **77**, 3865 (1996).
[39] J. Klimeš, D. R. Bowler, and A. Michaelides, Chemical accuracy for the van der Waals density functional, J. Phys. Condens. Matter **22**, 022201 (2009).
[40] F. Birch, Finite elastic strain of cubic crystals, Phys. Rev. **71**, 809 (1947).
[41] E. Hazrati, G. de Wijs, and G. Brocks, Li intercalation in graphite: A van der Waals density-functional study, Phys. Rev. B **90**, 155448 (2014).
[42] S. Singh, L. Lang, V. Dovale-Farelo, U. Herath, P. Tavadze, F.-X. Coudert, and A. H. Romero, Mechelastic: A Python library for analysis of mechanical and elastic properties of bulk and 2d materials, Comput. Phys. Commun. **267**, 108068 (2021).
[43] Y. Baskin and L. Meyer, Lattice constants of graphite at low temperatures, Phys. Rev. **100**, 544 (1955).
[44] A. Togo and I. Tanaka, First principles phonon calculations in materials science, Scr. Mater. **108**, 1 (2015).
[45] A. Togo, First-principles phonon calculations with phonopy and phono3py, J. Phys. Soc. Jpn. **92**, 012001 (2023).
[46] A. Togo, L. Chaput, and I. Tanaka, Distributions of phonon lifetimes in Brillouin zones, Phys. Rev. B **91**, 094306 (2015).
[47] L. Chaput, Direct solution to the linearized phonon Boltzmann equation, Phys. Rev. Lett. **110**, 265506 (2013).
[48] S.-i. Tamura, Isotope scattering of dispersive phonons in Ge, Phys. Rev. B **27**, 858 (1983).
[49] Y. Fei, A. Ricolleau, M. Frank, K. Mibe, G. Shen, and V. Prakapenka, Toward an internally consistent pressure scale, Proc. Natl. Acad. Sci. U.S.A. **104**, 9182 (2007).
[50] C. Prescher and V. B. Prakapenka, Dioptas: A program for reduction of two-dimensional X-ray diffraction data and data exploration, High Press. Res. **35**, 223 (2015).
[51] J. Buchen, H. Marquardt, K. Schulze, S. Speziale, T. Boffa Ballaran, N. Nishiyama, and M. Hanfland, Equation of state of polycrystalline stishovite across the tetragonal-orthorhombic phase transition, J. Geophys. Res. **123**, 7347 (2018).
[52] M. Hanfland, H. Beister, and K. Syassen, Graphite under pressure: Equation of state and first-order Raman modes, Phys. Rev. B **39**, 12598 (1989).
[53] P. Scherrer, Bestimmung der grosse und inneren struktur von kolloidteilchen mittels rontgenstrahlen, Nach Ges Wiss Gott. **2**, 8 (1918).
[54] A. C. Ferrari and J. Robertson, Interpretation of Raman spectra of disordered and amorphous carbon, Phys. Rev. B **61**, 14095 (2000).
[55] A. Goncharov, I. Makarenko, and S. Stishov, Graphite at pressures up to 55 GPa: Optical properties and Raman spectra, High Press. Sci. Technol. **4**, 345 (1990).
[56] A. Goncharov, Graphite at high pressures: Amorphization at 44 GPa, Int. J. High Press. Res. **8**, 607 (1992).